Meccanica (2011) 46: 113–129
DOI 10.1007/s11012-010-9394-9

PARALLEL MANIPULATORS

The Gantry-Tau parallel kinematic machine—kinematic and elastodynamic design optimisation

Ilya Tyapin · Geir Hovland

Received: 20 September 2009 / Accepted: 29 November 2010 / Published online: 24 December 2010

Abstract One of the main advantages of the Gantry-Tau machine is a large accessible workspace/footprint ratio compared to many other parallel machines. The optimal kinematic, elastostatic and elastodynamic design parameters of the machine are still difficult to calculate and this paper introduces an optimisation scheme based on the geometric and functional dependencies to define the workspace and first resonance frequency. This method assumes that each link and universal joint can be described by a mass-spring-damper model and calculates the transfer function from a Cartesian force or torque to Cartesian position or orientation. The evolutionary algorithm based on the complex search method is compared to the gradient-based search function in Matlab integrated optimisation toolbox. Kinematic design obtained by optimisation according to this paper gives a 2D workspace/footprint ratio more than 1.66 and first resonance frequency is more than 50 Hz with components of an existing lab prototype at the University of Agder, Norway.

Keywords PKM · Evolutionary · Design · Optimisation · Flexible · Dynamics · Model

I. Tyapin
Lulea University of Technology, Luleå, Sweden
e-mail: ilya.tyapin@ltu.se

G. Hovland (✉)
University of Agder, Grimstad, Norway
e-mail: geir.hovland@uia.no

1 Introduction

A generalised parallel kinematic manipulator (PKM) is a closed-loop kinematic chain mechanism where the end-effector is linked to the base by several independent kinematic chains [1]. It may consist of redundant mechanisms with more actuators than the number of controlled degrees of freedom of the end-effector. From the first ideas of [2] and [3], many PKMs and design methods have been developed.

The Tau family of PKMs was invented by ABB Robotics, see [4]. The Gantry-Tau was designed to overcome the workspace limitations while retaining many advantages of PKMs such as low moving mass, high stiffness and no link twisting or bending moments. For a given Cartesian position of the robot each arm has two solutions for the inverse kinematics, referred to left- and right-handed assembly modes. It is possible to operate the Gantry-Tau in both assembly modes without passing a singularity, see [5], and the workspace volume is significantly larger in comparison with both a serial Gantry-type robot and other PKMs with the same footprint and with only axial forces in the links of the arms. The intended applications of the robot are machining operations requiring a workspace equal to or larger than a typical serial-type robot's, but with higher stiffness. However, the robot can also be designed for very fast material handling, assembly and high precision processes such as laser cutting, water jet cutting and measurement.

In order to calculate the workspace one can employ discretisation, analytical and geometrical methods. A grid of nodes with position and orientation is defined for both discretisation and analytical methods. Then the kinematics is calculated for each node and it is straightforward to verify whether the kinematics can be solved and to check when joint limits are reached or link interference occurs. The discretisation algorithm is simple to implement but has some serious drawbacks. It is expensive in computations and results are limited to the nodes of the grid, [6]. Using geometrical methods the workspace can be calculated as an intersection of simple geometrical objects, [1], for example spheres. In this paper the maximum workspace is found as described in [1]. However, a fully geometric method to evaluate the unreachable areas on the boundary of the workspace caused by the end-effector's kinematics is presented. The collisions between the platform and support frame detected are also taken into account (also presented in [7]).

A frequency response model of a PKM over the entire working envelope is an essential tool when designing and dimensioning PKMs for high-speed machining and other applications. The flexibility of PKMs may cause structural resonance in the cutting process and mechanical interaction with the control system because of regenerative and modal chattering, which is the main concern in high-speed machining. Moreover, high structural resonance frequencies are needed to obtain a high bandwidth robot control. High bandwidth control means accurate and fast control of the tool position, speed and force.

The majority of published works about PKM structures has been on kinematics and singularity analysis. The study of dynamics of PKMs has received less attention, and flexible dynamics less than rigid-body dynamics. One of the first published works on flexible PKM dynamics was presented in [8]. A 3-DOF spatial PKM with three flexible links was modelled and simulated. The model took both axial forces and bending moments into account. The model was only simulated in the time-domain, and no frequency response data was presented.

Very little work has been presented on flexible dynamic modelling of Hexapod PKMs, for example [9]. In [10] the Lagrange equations for flexible Stewart manipulators using tensor representation has been modelled as a mass-spring-damper. In [11] a flexible model using finite elements is presented. Two recent publications dealing with modelling of flexible PKMs were presented in [12] and [13]. Both papers modelled Tripod PKMs with flexible links. Because of the Tripod structure, the flexible dynamic models must take link bending and twisting moments as well as axial forces into account. [13] presents a frequency response diagram of a Tripod and is able to quantify the lowest resonance frequency of the machine over the entire working envelope. In [14] a new and general approach for calculating the dynamic frequency response of PKM with six links is presented. This method exploits the fact that this type of PKMs only experiences axial link forces and the method is significantly faster than general Finite Element Method (FEM) used for other PKM structures which also take link bending and twisting moments into account. Another interesting work related to the Gantry-Tau is presented in [15]. The authors used the Modelica object-oriented programming language to define the Gantry-Tau dynamic model based on non-parallel actuator axis but the static matrix and flexible links design are not used in [15]. A dynamic model optimisation is also presented in [15].

In [14] the variations of link stiffness and mass as a function of link length were ignored because of the assumption that the joint stiffnesses are being much lower than the link stiffnesses. In this paper the link stiffness values are functions of the link lengths and link stiffness is found for each link. As a result, the method presented in this paper is more accurate and 12 times faster. The time saving is possible because the static matrix and Jacobian matrices for the Laplace transform are found from a functional dependency, where the coefficients of the functions are found analytically. In addition, the workspace is discretised in one axis only. In [14] the static matrix had to be recalculated for every point of the workspace and for different frequencies ω of the Laplace operator.

As stated in [16] the optimisation process may consist of the following stages: translate the end-user requirements into numerical indices, choose the structure and choose the dimensioning. The transformation of the user's requirements into numerical performances is given by number of DOF, workspace description, geometry and mass of load, footprint of the robot, actuators, joints, stiffness, position accuracy, internal sensors, dynamics and cost [16]. The priority levels have to be chosen for all performances.

The workspace is one of the most important indices in design of a parallel manipulator. However, a parallel manipulator designed to maximise workspace may not be a good design in practice, because it may have undesirable kinematic characteristics such as poor dexterity or manipulability. In [17] this problem was investigated for a 3-DOF translational parallel manipulator. In order to avoid the undesirable effects of workspace maximisation, researchers introduced other performance criteria into the optimal design problem. Gosselin and Angeles designed a planar [18] and a spherical [19] 3-DOF parallel manipulator by maximising the workspace volume, while taking into account the isotropy index. In [17] total volume of well-conditioned workspace optimisation is presented. The well-conditioned workspace is given by the integral of inverse condition number of the kinematic Jacobian matrix over the workspace. In [20] the design of a 3-DOF purely translational parallel mechanism is presented. The optimisation is based on the use of the performance chart for a good conditioned workspace, a global conditioning index, and a global stiffness index. In [21] a linear combination of measures on manipulability and workspace volume in the objective function is presented. The design optimisation problem is described as a multi-objective optimisation problem in [21]. In [22] the design optimisation for 3-DOF PKM is conducted on the basis of a prescribed Cartesian workspace with prescribed kinetostatic performances. In [23] performance evaluation and dimensional synthesis based on the kinematic optimisation for the planar parallel manipulator with a new index of transmissibility was presented. In [24] an optimal design of PKM is based on a search of optimal geometry that maximises the effective regular workspace and includes constraints on joint limits and link interference. In this paper the optimisation problem includes the collisions free workspace, joint angle limits, dynamics performances, installation space and user's requirements. The use of evolutionary approach to optimise the parallel kinematic structure, where the optimal design is found as a trade-off between the kinematics and dynamics performances is also presented in this paper.

In [25] the first implementation of the multi-objective evolutionary algorithm is presented. Since then, a considerable amount of research has been done in this area. For example, in [26] evolutionary multi-objective algorithm with preference is proposed. The constraints are considered as a new objective, a prior method including the user preferences is adopted, and a multi-criteria decision aid method to rank the members of the population is used in [26]. A detailed review of various constraint handling techniques used with evolutionary algorithms is presented in [27]. The most common approach to deal with constrains is the use of penalty functions, where the amount of constraint violations is used to penalise an infeasible solution and feasible solutions are favoured by the selection process.

The complex search method was used for the mechanical design optimisation in [28] and [29]. In [28] a mechanical design optimisation of a hydraulically actuated manipulator is presented. The main objective is minimising the energy consumption with side constraints on stability, response time and load dependency. The initial population has 30 designs and the optimum design is found in 250 iterations. In [29] a multi-objective design optimisation of a servo-robot for pallets handling is presented. The objectives are the cost and speed. The accuracy of the tool point, an expected life of the planetary gears and the welded structure, vibrations and thermal conditions of the servo motors are the main side constraints. Discrete design variables are originally handled by a mapping technique. The optimum design was found in 50 iterations with the initial population of 10. In [30] the complex search method is used to optimise kinematic and elastostatic properties of the 3-DOF Gantry-Tau manipulator, where a trade-off between workspace to installation space ratio and required level of Cartesian stiffness is found. Compared to this paper, the dynamic performances are not taken into account in [30].

Brief descriptions of the kinematics and workspace evaluation are presented in Sects. 2 and 3. The statics and dynamics are explained in Sects. 4 and 5. The first resonance frequency calculation method based on the Laplace transform is also presented in Sect. 5. The optimisation problem formulation is presented in Sect. 6. The results are given in Sect. 7 and conclusions are presented in Sect. 8.

2 Kinematic description

In this paper we consider the triangular-link version of the Gantry-Tau structure with no telescopic links,

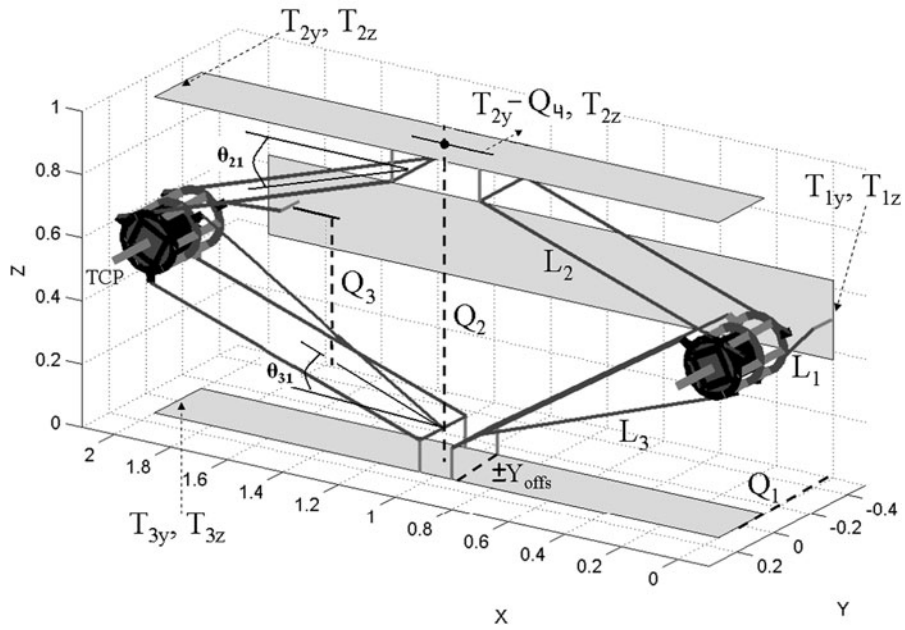

Fig. 1 The 3-DOF reconfigurable Gantry-Tau robot in left- and right-hand assembly modes. (T_{iy} T_{iz}) are actuator positions, Q_1–Q_4 are optimisation variables, L_1–L_3 are the arm lengths and θ is a joint angle limit

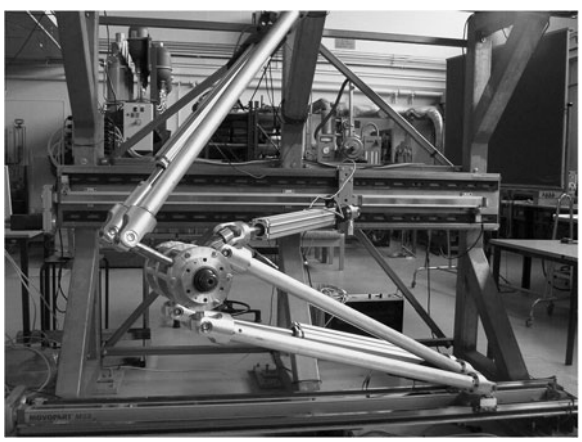

Fig. 2 Prototype of a Gantry-Tau with a triangular-mounted link pair

which is illustrated in Figs. 1 and 2. The architecture consists of a fixed base and a mobile platform connected by three arms. Figure 1 shows the PKM structure in both the left- and right-handed assembly modes. As for the basic Gantry-Tau structure, the position of one end of each arm (lengths L_1, L_2 and L_3) is controlled by a linear actuator with actuation variables q_1, q_2 and q_3, see Fig. 2. The actuators are aligned in the direction of the global X coordinate. The actuator track locations are fixed in the Y and Z directions and locations are denoted as T_{1y}, T_{1z}, T_{2y}, T_{2z}, T_{3y} and T_{3z}, respectively. The dimensioning of the PKM's support frame is given by the four variables Q_1, Q_2, Q_3 and Q_4 as illustrated in Fig. 1, where Q_1 is the depth, Q_2 is the height of the support frame, Q_3 is the Z-coordinate of the actuator T_1 and Q_4 is the Y-coordinate of the actuator T_2. The width of the machine in the X direction is given by the length of the actuators or specified by the user.

Figures 3 and 4 show the manipulated platform and fixed kinematic parameters of the moving platform, which are not included into the design optimisation scheme. L_p is the platform length, R_p is the platform radius, L_{tool} is the tool length, L_{pin} is the length from the platform circle of radius R_p to the connection point of the universal joints, L_b is the length from the connection point to the centre of the joint. The points A, B, C, D, E and F are the link connection points. The arm with one single link connects the actuator q_1 with platform point F. The arm with two links connects actuator q_2 with the platform points A and B. The arm with three links connects actuator q_3 with the platform points C, D and E. The triangular pair is connected to points C and E. The **TCP** of the robot is located at the tip of the milling tool. Each link

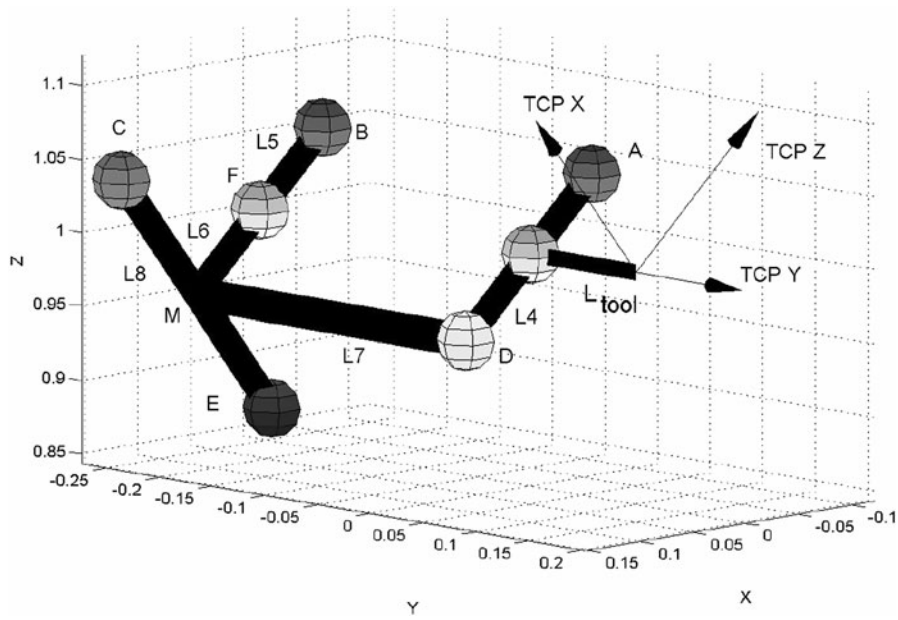

Fig. 3 The manipulated platform of the Gantry-Tau robot. A–F are the points on the platform, L_4–L_8 are the distances between the points

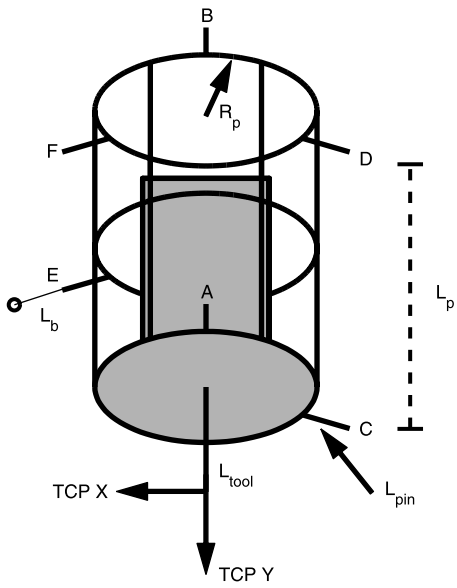

Fig. 4 Kinematic platform parameters. L_p is the platform length, R_p is the platform radius, L_{tool} is the tool length, L_{pin} is the length from the platform circle of radius R_p to the connection point of the universal joints, L_b is the length from the connection point to the centre of the joint

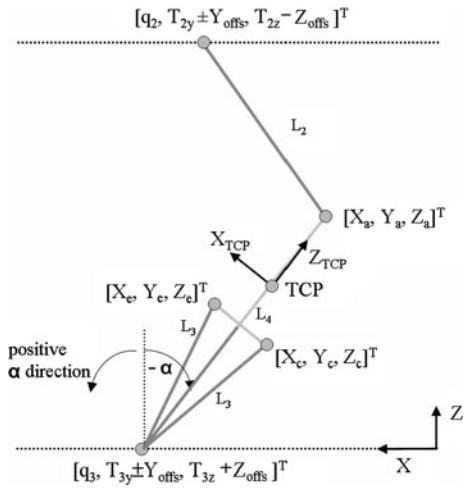

Fig. 5 Robot's kinematic parameters in the XZ-plane. α is the platform orientation angle, $(q_i\ T_{iy}\ T_{iz})$ is the actuator position, $[X_a\ Y_a\ Z_a]$ are the point A coordinates in a world frame, X_{TCP} and Z_{TCP} are TCP coordinate axis

has a passive 2D universal joint at one end and a passive 3D joint at the other end. In Fig. 5 the manipulated platform orientation angle α around Y-axis is shown. The prototype of the 3-DOF Gantry-Tau with a triangular-mounted link pair built at the University of Agder (Norway) is shown in Fig. 2. The structure and full kinematics of the Gantry-Tau is presented in [7].

3 Workspace

A fully geometric approach to define the maximum workspace of the Gantry-Tau is based on approach presented in [1] and full description is given in [7].

Figure 6 shows three circles in the YZ-plane, one for each arm, while Fig. 7 shows the entire workspace in the XZ-plane. The centres of the circles 1, 2 and 3 are located at the points $((T_{1y} + L_p + L_{tool})\ (T_{1z} + R_p + L_{pin} + \frac{L_b}{2}))$, $((T_{2y} + Y_{off} + L_{tool})\ (T_{2z}))$ and $((T_{3y} + Y_{off} + L_{tool})\ (T_{3z}))$ respectively, where Y_{off} is shown in Fig. 1. The radii of the circles equal the arm lengths and distance from the connection point on the platform to the **TCP** in the XZ-plane. The **TCP** can only reach points inside of all circles. Figure 6 also contains three solid lines in the YZ-plane. The **TCP** is not allowed to move outside of these lines because they indicate the positions of the support framework. The valid **TCP** positions are illustrated in grey colour in Fig. 6.

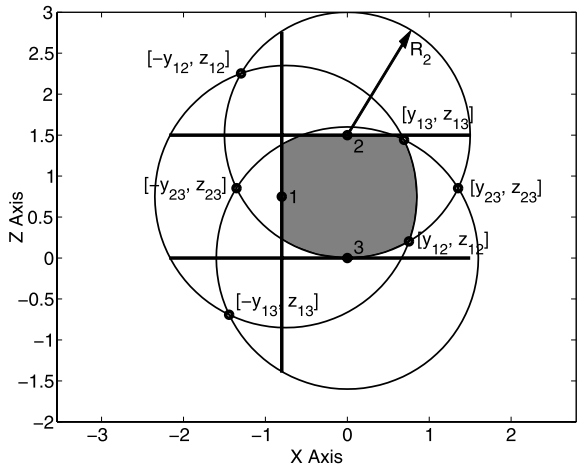

Fig. 6 The cross-sectional workspace area of the Gantry-Tau in the YZ-plane. *Three circles* define the maximum workspace (*grey area*). Points *1, 2, 3* are actuator positions, $[y_{ij}\ z_{ij}]$ are cross-points between the circles i and j, R_2 is the radius of circle *2*

The maximum workspace is limited by the collisions between the links. The distance between two line segments is defined as the minimum distance between two points on these segments. Link collisions occur when the distance between two points on the links is less than the sum of radii of these links. The links of the manipulator are assumed to be cylindrical elements. The Gantry-Tau link collisions detection method presented in [7] is based on the conditional equations (boundaries) search and not presented in this paper because of limited space. The functional dependency analysis is applied to the condition equations.

The collisions between the support frame and manipulated platform reduce the maximum workspace. In Fig. 8 the square in the middle defines the user's specified workspace, where all user's requirements are met. The areas where the collisions occur are shown in a grey colour. The lengths of these areas h_{a1}, h_{a2}, h_{a3} and total area A_U are expressed as follows.

$$A_U = A_{U1}(h_{a1}) + A_{U2}(h_{a2}) + A_{U3}(h_{a3}) \tag{1}$$

$$h_{a1} = L_p + L_{tool} \tag{2}$$

$$h_{a2} = R_p^* \cos(\alpha_{min}) \tag{3}$$

$$h_{a3} = \left(\sqrt{L_3^2 - R_p^{*2}\sin^2\left(\frac{2\pi}{3}\right)} + R_p^* \cos\left(\frac{2\pi}{3}\right)\right)\frac{R_p^* \sin(\frac{2\pi}{3})}{L_3} \tag{4}$$

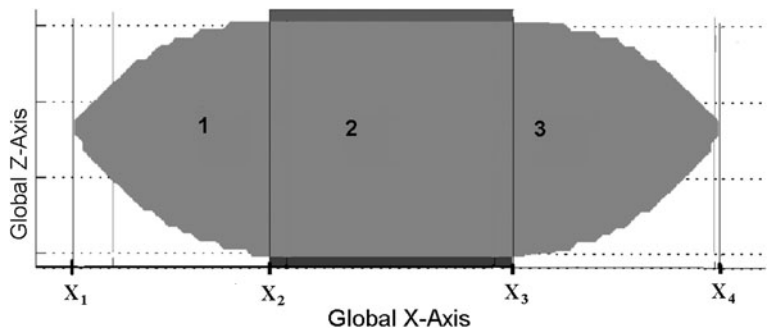

Fig. 7 The workspace area of Gantry-Tau machine in the XZ-plane when it is reconfigured to work in both positive and negative x-direction. In section *2* the workspace is fixed and in *1* and *3* it shrinks

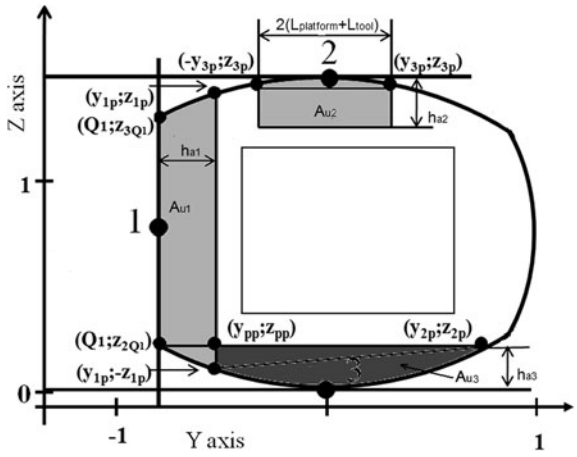

Fig. 8 Illustration of the areas where the collisions between the platform and support frame are detected (*grey areas*). The *square* in the *middle* is an example of a user's specified workspace. Cross-points between the circles and lengths h_{a1}, h_{a2}, h_{a3} are also shown

$$\alpha_{min} = \frac{\pi}{2} - \arcsin\left(\frac{Q_2}{den}\right) \quad \text{if } (Q_2 < den) \tag{5}$$

$$\alpha_{min} = 0 \quad \text{if } Q_2 \geq den \tag{6}$$

$$den = \sqrt{L_3^2 - R_p^{*2}\sin^2\left(\frac{2\pi}{3}\right)} + R_p^* \sin\left(\frac{2\pi}{3}\right) + R_p^* \tag{7}$$

$$R_p^* = L_{pin} + R_p + \frac{L_b}{2} \tag{8}$$

where α_{min} is a minimum possible platform orientation angle for the current design. For more details about the workspace evaluation, link collisions and collisions between the platform and support frame refer to [7].

4 Static analysis

This section contains equations and matrices which are required for the dynamic analysis in Sect. 5.

$$\mathbf{X} = [X\ Y\ Z]^T \qquad \theta = [\alpha\ \beta\ \gamma]^T$$

$$\mathbf{F} = [F_x\ F_y\ F_z]^T \qquad \mathbf{M} = [M_x\ M_y\ M_z]^T$$

$$\mathbf{L} = [l_1\ l_2\ l_3\ l_4\ l_5\ l_6]^T \qquad \mathbf{F}_a = [F_1\ F_2\ F_3\ F_4\ F_5\ F_6]^T$$

where X, Y, Z are the Cartesian **TCP** coordinates, α, β, γ are the Cartesian **TCP** orientation angles, l_i are the link lengths and F_i are link forces where $i = 1, \ldots, 6$. F_x, F_y and F_z are the external Cartesian forces acting on the **TCP** and M_x, M_y and M_z are the external Cartesian torques acting on the **TCP**. The relationship between the **TCP** forces and link forces are.

$$\mathbf{F} = \sum_{i=1}^{6} F_i \mathbf{u}_i \qquad \mathbf{M} = \sum_{i=1}^{6} F_i \mathbf{A}_i \times \mathbf{u}_i \tag{9}$$

where $\mathbf{u_i}$ is a unit vector in the direction of link i and $\mathbf{A_i}$ is a vector pointing from the **TCP** to the end-point of link i on the platform. The two equations above can be rewritten using the 6×6 statics matrix $\mathbf{H}$.

$$\begin{bmatrix} \mathbf{F} \\ \mathbf{M} \end{bmatrix} = \mathbf{H}\mathbf{F}_a \qquad \begin{bmatrix} \Delta\mathbf{X} \\ \Delta\theta \end{bmatrix} = \mathbf{J}\Delta\mathbf{L} \tag{10}$$

The Jacobian matrix of the PKM relates changes in Cartesian position $\Delta\mathbf{X}$ and orientation $\Delta\theta$ with changes in the link lengths $\Delta\mathbf{L}$ as shown in (10) (right). [31] show the duality between the statics and the link Jacobian for PKMs, i.e.

$$\mathbf{H}^{-1} = \mathbf{J}^T \tag{11}$$

Based on the duality result, the Cartesian stiffness matrix $\boldsymbol{K}$ can be derived as a function of the statics matrix as follows.

$$\begin{bmatrix} \mathbf{F} \\ \mathbf{M} \end{bmatrix} = \boldsymbol{K} \begin{bmatrix} \Delta\mathbf{X} \\ \Delta\theta \end{bmatrix} = \mathbf{H}\mathbf{F}_a = \mathbf{H}\boldsymbol{K}_L\Delta\mathbf{L}$$

$$\mathbf{H}\boldsymbol{K}_L\mathbf{J}^{-1}\begin{bmatrix} \Delta\mathbf{X} \\ \Delta\theta \end{bmatrix} = \mathbf{H}\boldsymbol{K}_L\mathbf{H}^T\begin{bmatrix} \Delta\mathbf{X} \\ \Delta\theta \end{bmatrix}$$

$$\Rightarrow \quad \mathbf{K} = \mathbf{H}\boldsymbol{K}_L\mathbf{H}^T \tag{12}$$

where $\boldsymbol{K}_L$ is a 6×6 diagonal matrix with the individual link stiffnesses along the diagonal. Note that in [32] a Congruence Transformation Matrix $\mathbf{K_g}$ is defined, which represents the changes in geometry through the differential Jacobian matrix, and externally applied forces. In this paper, the $\mathbf{K_g}$ matrix is not taken into account, since the joint stiffness $\mathbf{K}_\theta$ dominates for small external forces. The result in (12) has the benefit that no matrix inversions are required to calculate the Cartesian stiffness at X, Y and Z coordinates, including coordinates where $\mathbf{H}$ is singular.

The elements of the matrix $\mathbf{H}$ are the X, Y and Z components of the vectors pointing from the actuator positions to the points A, B, C, D, E, F on the

platform and X, Y and Z components of the cross-products of these vectors and vectors pointed from the **TCP** to the points on the platform, see Fig. 3. The vectors pointing from the actuator positions to the points on the platform are given below

$$\mathbf{A} = [A_x\ A_y\ A_z]^T \qquad \mathbf{B} = [B_x\ B_y\ B_z]^T$$
$$\mathbf{C} = [C_x\ C_y\ C_z]^T \qquad \mathbf{D} = [D_x\ D_y\ D_z]^T$$
$$\mathbf{E} = [E_x\ E_y\ E_z]^T \qquad \mathbf{F} = [F_x\ F_y\ F_z]^T$$

The 6×6 static matrix $\mathbf{H}$ is given below.

$$\mathbf{H} = \begin{pmatrix} A_x & \dots & F_x \\ A_y & \dots & F_y \\ A_z & \dots & F_z \\ (\mathbf{A} \times \mathbf{A_{TCP}})_x & \dots & (\mathbf{F} \times \mathbf{F_{TCP}})_x \\ (\mathbf{A} \times \mathbf{A_{TCP}})_y & \dots & (\mathbf{F} \times \mathbf{F_{TCP}})_y \\ (\mathbf{A} \times \mathbf{A_{TCP}})_z & \dots & (\mathbf{F} \times \mathbf{F_{TCP}})_z \end{pmatrix} \tag{13}$$

where $\mathbf{A_{TCP}} \dots \mathbf{F_{TCP}}$ are vectors pointed form **TCP** to the points on the platform.

According to the kinematic description presented in [7], the vectors from the actuators to the points on the platform are expressed as follows.

$$\begin{aligned}
\mathbf{A} &= [(a_x C + a_z S + dX_1)_n\ (a_y + dY_1)_n \\
&\quad (a_z C - a_x S + dZ_1)_n]^T \\
\mathbf{B} &= [(b_x C + b_z S + dX_2)_n\ (b_y + dY_2)_n \\
&\quad (b_z C - b_x S + dZ_2)_n]^T \\
\mathbf{C} &= [(c_x C + c_z S + dX_3)_n\ (c_y + dY_3)_n \\
&\quad (c_z C - c_x S + dZ_3)_n]^T \\
\mathbf{D} &= [(d_x C + d_z S + dX_4)_n\ (d_y + dY_4)_n \\
&\quad (d_z C - d_x S + dZ_4)_n]^T \\
\mathbf{E} &= [(e_x C + e_z S + dX_5)_n\ (e_y + dY_5)_n \\
&\quad (e_z C - e_x S + dZ_5)_n]^T \\
\mathbf{F} &= [(f_x C + f_z S + dX_6)_n\ (f_y + dY_6)_n \\
&\quad (f_z C - f_x S + dZ_6)_n]^T
\end{aligned} \tag{14}$$

where $C = \cos\alpha$, $S = \sin\alpha$, $dX_i = X - T_{ix}$, $dY_i = Y - T_{iy}$, $dZ_i = Z - T_{iz}$, $[a_x a_y a_z]$, $[b_x b_y b_z]$, $[c_x c_y c_z]$, $[d_x d_y d_z]$, $[e_x e_y e_z]$, $[f_x f_y f_z]$ are the coordinates of the points A, B, C, D, E, F in the **TCP** coordinate frame, subscript $_n$ indicates normalised vector's components. The $\cos\alpha$ and $\sin\alpha$ are given as follows.

$$\cos\alpha = \frac{T_{3z} - Z}{\sqrt{L_{3m}^2 - (Y + M_y - T_{3y})^2} + \sqrt{M_x^2 + M_z^2}} \tag{15}$$

$$\sin\alpha = \sqrt{1 - \cos^2\alpha} \tag{16}$$

L_{3m} is the middle length of the triangular-mounted arm 3. M_x, M_y, M_z are coordinates of a midpoint M between the triangular link coordinates C and E on the platform, see Fig. 3. In [7] the YZ functional dependency to define the elements of the static matrix is presented.

5 Dynamics model

The flexible model of a single link in Fig. 9 assumes that the actuator is rigid and stationary. Figure 10 shows the flexible model for all six links. The parameters k_j and damper z_j represent the flexibility in the universal joint. The mass m_j is the total weight of the joint. In Fig. 9 the platform mass M_{TCP} equals the platform mass plus six halves of the joint masses, i.e. $M_{TCP} = m_2 + 3m_j$. The mass M_a equals the sum of the masses of the two joint halves and the total weight of the link, i.e. $M_a = m_a + m_j$. Isolating the dynamics for link i and then the platform, the flexible equations of motion become

$$\begin{aligned}
M_a \ddot{a}_i &= -k_1 a_i - z_1 \dot{a}_i + (l_i - a_i)k_2 \\
&\quad + (\dot{l}_i - \dot{a}_i)z_2
\end{aligned} \tag{17}$$

$$\begin{aligned}
M_{TCP}\ddot{\boldsymbol{X}} &= \boldsymbol{F} + \sum_j (a_j - l_j)k_2 \boldsymbol{u}_j \\
&\quad + \sum_j (\dot{a}_j - \dot{l}_j)z_2 \boldsymbol{u}_j
\end{aligned} \tag{18}$$

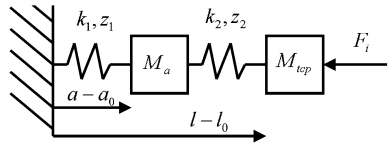

Fig. 9 Simplified flexible link model

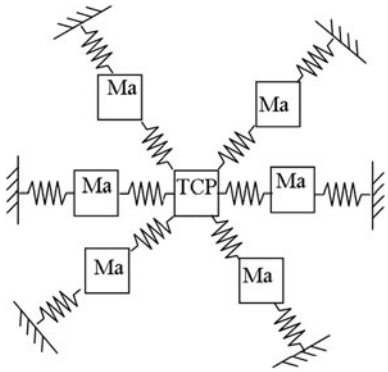

Fig. 10 Flexible model of 6-link PKM

$$I_{TCP}\ddot{\boldsymbol{\theta}} = \boldsymbol{M} + \sum_j (a_j - l_j)k_2 \boldsymbol{A}_j^* + \sum_j (\dot{a}_j - \dot{l}_j)z_2 \boldsymbol{A}_j^* \tag{19}$$

$$\boldsymbol{A}_j^* = (\boldsymbol{A}_j \times \boldsymbol{u}_j)$$

where $\boldsymbol{u}_j$ and $\boldsymbol{A}_j$ were introduced in (9). For small motions, the equations above are linear in the variables a and l as functions of the external **TCP** forces $\boldsymbol{F}$ and torques $\boldsymbol{M}$ and the **TCP** linear and rotary accelerations. By introducing the Laplace transform, the 18 equations above can be written on matrix form as follows.

$$\begin{bmatrix} A & -B \\ C & D \end{bmatrix} \begin{bmatrix} a_i \\ l_i \end{bmatrix} = \begin{bmatrix} \mathbf{0} \\ \boldsymbol{F} \\ \boldsymbol{M} \end{bmatrix} \tag{20}$$

where $\mathbf{0}$ is a 6×1 zero vector. The matrix elements A, B, C and D are functions of the Laplace transform, the masses and the flexibility parameters. For example,

$$A = \left(M_a s^2 + (z_1 + z_2)s + k_1 + k_2\right)\boldsymbol{I}_6 \tag{21}$$

$$B = (z_2 s + k_2)\boldsymbol{I}_6 \tag{22}$$

where $\boldsymbol{I}_6$ is a 6×6 identity matrix. In addition to the link masses, springs and dampers, the 6×6 submatrices C and D will also contain platform parameters, such as the platform weight and inertia. The Cartesian position vector $\boldsymbol{X}$ and the orientation vector $\boldsymbol{\theta}$ are replaced by a and l by using the Jacobian matrix.

Hence, the 12 unknown parameters a_i and l_i can be solved by inverting the matrix in (20). If we know the direct link Jacobian matrix of the PKM, the Cartesian velocities can be calculated as follows.

$$\frac{d}{dt}\begin{pmatrix} \boldsymbol{X} \\ \boldsymbol{\theta} \end{pmatrix} = \boldsymbol{J}\dot{\boldsymbol{L}} \quad \rightarrow \quad s\boldsymbol{I}_6 \begin{bmatrix} \boldsymbol{X} \\ \boldsymbol{\theta} \end{bmatrix} = s\boldsymbol{I}_6 \boldsymbol{J}\boldsymbol{L} \tag{23}$$

where $\boldsymbol{L} = [l_1, \ldots, l_6]^T$. The final transfer functions of the PKM from Cartesian forces or moments to Cartesian positions or orientation can then be derived from (20), (23).

$$\frac{\boldsymbol{X}_i}{F_j}(s) = \frac{\boldsymbol{X}_i}{l_i}(s)\frac{l_i}{F_j}(s) \qquad \frac{\boldsymbol{\theta}_i}{M_j}(s) = \frac{\boldsymbol{\theta}_i}{l_i}(s)\frac{l_i}{M_j}(s) \tag{24}$$

The first resonance frequency calculation algorithm consists of a few stages.

Stage 1. All constants are found in this stage. Note, that constants are not ω, Y or Z dependent. M_{TCP}—the platform mass, M_a—the mass of the total weight of a link plus masses of the two joint halves, k_j—the joint stiffness, Sec_i—the section of the link (m^2), ε—Young's modulus, J_{pl}—an inertia matrix of the platform and z_1, z_2-damping ratio.

According to Hooke's law, the link stiffness are given below.

$$k_{1i} = \frac{2\varepsilon k_j Sec_i}{2\varepsilon Sec_i + k_j L_i}; \quad k_{2i} = k_{1i} \tag{25}$$

where L_i is the link length, $i = 1, \ldots, 6$, Sec_i is an area of the link section.

Stage 2. In this stage the equations for a_i through l_i is found from (17), (20).

$$a_i = BA^{-1}l_i \tag{26}$$

where A and B were found before, see (21)–(22).

Stage 3. A vector $L(s)$ as a function of the Laplace operator s is found in this stage. Firstly, forces and moments in (18) and (19) are divided by $M_{TCP}s^2$ and $I_{TCP}s^2$ to get the **TCP** 3-DOF position **X** and orientation $\boldsymbol{\theta}$ vectors.

$$\begin{aligned} U_i &= \frac{(a_i - l_i)(k_2 + z_2 s)}{s^2 M_{TCP}}[H_{1i} \quad H_{2i} \quad H_{3i}]^T \\ V_i &= \frac{(a_i - l_i)(k_2 + z_2 s)}{s^2}[H_{4i} \quad H_{5i} \quad H_{6i}]^T \end{aligned} \tag{27}$$

where $i = 1, \ldots, 6$ according to the links, H_{1i}, H_{2i}, H_{3i}, H_{4i}, H_{5i}, H_{6i} are elements of a static matrix **H**, U is (18) divided by $M_{TCP}s^2$ and V is (19) divided by $I_{TCP}s^2$. Note, that elements **F** and **M** are skipped

in (27). According to (26) the elements a_i are replaced in (27).

$$U_i = l_i \frac{(BA^{-1}-1)(k_2+z_2 s)}{s^2 M_{TCP}}[H_{1i} \quad H_{2i} \quad H_{3i}]^T$$
$$V_i = l_i \frac{(BA^{-1}-1)(k_2+z_2 s)}{s^2}[H_{4i} \quad H_{5i} \quad H_{6i}]^T \tag{28}$$

Secondly, a vector $L(s) = [l_1, \ldots, l_6]$ is found from (23). The Jacobian $\mathbf{J}$ is the transpose of the static matrix $\mathbf{H}$. A vector $L(s)$ consists of 6 unknown variables and the solution is a 6×6 matrix L_s.

$$L_s = \mathbf{H}^T \begin{pmatrix} U_{h1} & U_{h2} & \ldots & U_{hi} \\ V_{h1} & V_{h2} & \ldots & V_{hi} \end{pmatrix} \tag{29}$$

where U_h and V_h are 3×6 matrixes.

$$U_{hi} = \frac{1}{s^2 M_{TCP}}[F_x \quad F_y \quad F_z]^T + U_i \tag{30}$$

$$V_{hi} = J_{pl}\frac{1}{s^2}[M_x \quad M_y \quad M_z]^T + V_i \tag{31}$$

Three elements (L_{s11}, L_{s12}, L_{s21},) of the matrix L_s are given below. Other 33 elements are found in a similar way.

$$L_{s11} = \frac{H_{11}}{C_3} + l_1(-1 + C_1 H_{11}^*) + C_2 H_{11}^{**} \tag{32}$$

$$L_{s12} = \frac{H_{12}}{C_3} + l_2 C_1 H_{12}^* + C_2 H_{12}^{**} \tag{33}$$

$$L_{s21} = \frac{H_{11}}{C_3} + l_1 C_1 H_{12}^* + C_2 H_{12}^{**} \tag{34}$$

$$H_{11}^* = H_{11}^2 + H_{21}^2 + H_{31}^2 \tag{35}$$

$$H_{11}^{**} = \frac{H_{41}^2}{J_{pl11}} + \frac{H_{51}^2}{J_{pl22}} + \frac{H_{61}^2}{J_{pl33}} \tag{36}$$

$$H_{12}^* = H_{11}H_{12} + H_{21}H_{22} + H_{31}H_{32} \tag{37}$$

$$H_{12}^{**} = \frac{H_{41}H_{42}}{J_{pl11}} + \frac{H_{51}H_{52}}{J_{pl22}} + \frac{H_{61}H_{62}}{J_{pl33}} \tag{38}$$

where C_1 and C_2 are help variables and are given below.

$$C_1 = -\frac{M_a z_2 s^3 + (M_a k_2 + z_1 z_2)s^2 + (z_1 k_2 + k_1 z_2)s + k_1 k_2}{M_{TCP}(M_a s^4 + (z_1+z_2)s^3 + (k_1+k_2)s^2)} \tag{39}$$

$$C_2 = C_1 M_{TCP} \qquad C_3 = s^2 M_{TCP} \tag{40}$$

According to (34),

$$-\frac{H_{12}}{C_3} = l_2 C_1 H_{12}^* + C_2 H_{12}^{**} \tag{41}$$

$$-\frac{H_{1i}^T}{C_3} = \mathbf{S} * l_i \quad \Rightarrow \quad L(s) = -\frac{\mathbf{S}^{-1} H_{1i}^T}{C_3} \tag{42}$$

where $\mathbf{S}$ is a 6×6 matrix and l_i, H_{1i} are 6×1 vectors. The elements of $\mathbf{S}$ matrix are the elements of L_s matrix without $\frac{H_{1i}}{C_3}$ and divided by l_i. $\mathbf{S}$ is found from all 36 elements of L_s. l_i is a function of the Laplace transform. H_{1i} is a vector with elements equal to the elements of the first row of the static matrix $\mathbf{H}$.

Stage 4. The Cartesian **TCP** position vector as a function of the Laplace operator s is found in this stage and an equation is given below.

$$X(s) = (\mathbf{H^{-1}})^T L(s) \tag{43}$$

where $L(s) = [l_1, l_2, \ldots, l_6]$.

Stage 5. The first resonance frequency is found in this stage as the first maximum of the amplitude response γ_k for the given workspace cell k.

$$\gamma_k = |X(j\omega)| \tag{44}$$

The Laplace operator s in (44) is replaced by $j\omega$, where j is the complex unity and ω is a frequency. The first resonance frequency is found by a search algorithm using the amplitude response.

A flowchart of the first resonance frequency calculation algorithm is shown in Fig. 11.

The YZ functional dependency is used to find the elements of matrix S, see (42). The elements of the matrix $\mathbf{S}$ consist of two parts ω dependent C_1, C_2, see (41) and (42), and YZ dependent elements of the static matrix $\mathbf{H}$. The number of calculations are reduced because the differences between the elements S_{12} and S_{21} are ω dependent elements C_1 and C_2. YZ dependent parts are found once for the elements S_{12} and S_{21} and ω dependent parts are taken into account after that.

When all YZ dependent parts of the matrix $\mathbf{S}$ are found, the ω dependency is taken into account. Note, that elements C_1, C_2 of the matrix $\mathbf{S}$ have constant parts as coefficients before the Laplace transform s. The matrix $\mathbf{S}$ is recalculated for the different frequencies ω without recalculating the YZ dependent part of the equations. In conclusion, there are two functional dependencies in the first resonance frequency calculation algorithm. Both of them are found separately.

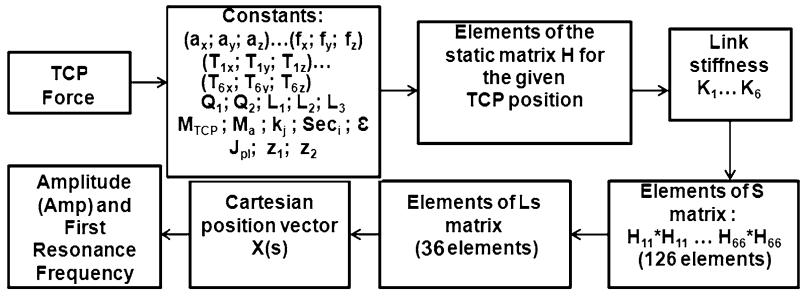

Fig. 11 The flowchart of the first resonance frequency calculation algorithm

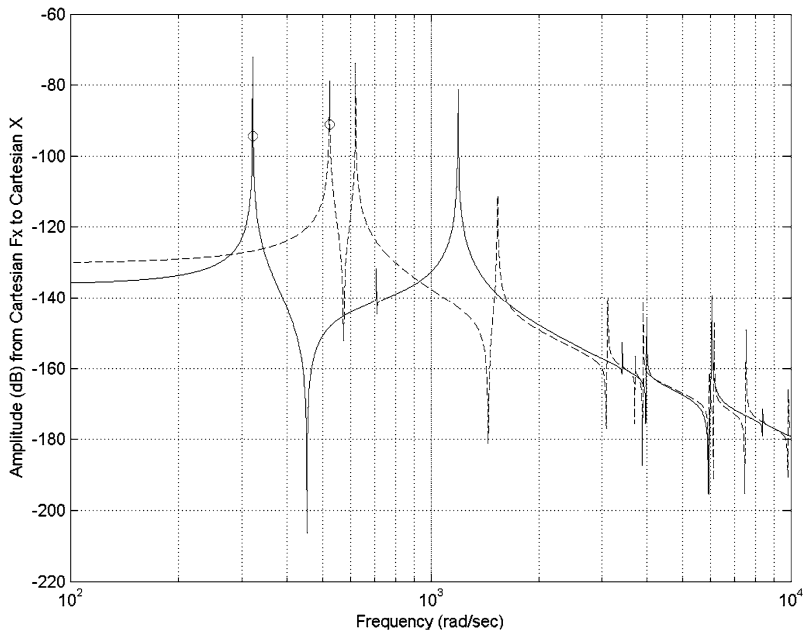

Fig. 12 Example of frequency response curves for the fixed-length version of the Gantry-Tau

Firstly, YZ dependent elements of the **S** matrix are found. Secondly, ω dependent elements of matrix **S** can be found, because YZ dependent elements are independent of ω.

Figure 12 shows two examples of the frequency response curves that are generated by the methods presented in this section. The solid curve shows the amplitude response from a Cartesian force in the X-direction to Cartesian position in the X-direction at $X = 1.0$, $Y = 0.0$ and $Z = 0.5$. The dotted curve shows the same response at $X = 1.0$, $Y = 0.8$ and $Z = 0.5$. The first resonance frequency occurs at 322 rad/sec or 51.2 Hz and 525 rad/sec or 83.6 Hz, respectively, for the two selected locations. The minimum, maximum and average first resonance frequency of the Gantry-Tau in the entire workspace and the best 70% of the workspace are given in Table 1.

Table 1 Resonance frequencies of the 3-DOF Gantry-Tau in the entire workspace and the best 70% workspace

	Min	Max	Avg
Entire workspace	47.54	102.85	60.61
Best 70 percent workspace	53.84	102.85	64.43

A map of the first resonance frequency as a function of the Y and Z coordinates for the Gantry-Tau is shown in Fig. 13. The frequency response data generated by the new method presented in this section have been verified against calculations from a FE soft-

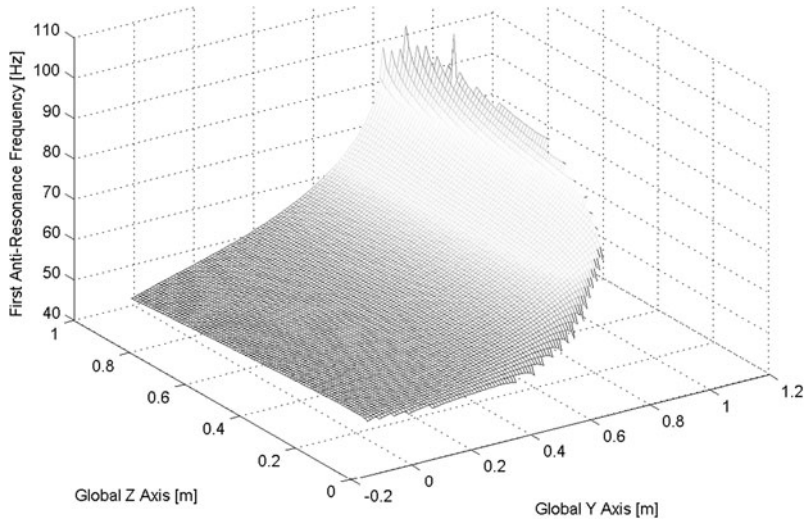

Fig. 13 First resonance frequency as function of the Y and Z coordinates at $X = 1.0$

Table 2 First resonance frequency computation time for three different methods

Method	Time
Finite Element Method	5600
Method in [14]	12
Functional Dependency	1

ware package (Strand7). For a set of 10 locations in the workspace of the Gantry-Tau, the method in this section generates the same results as the FE package and the method is also significantly faster. The maps in Fig. 13 can be generated approximately in the same time as it takes to set up and calculate one resonance frequency in a FE package.

Table 2 shows the computational requirements for the three different approaches on the triangular version of the 3-DOF Gantry-Tau PKM. The first resonance frequency calculation covers 70% of the entire workspace of the PKM. The method based on the functional dependency is 5600 times faster than the Finite Element Method. The computational time has been normalised to 1 for the third approach.

6 3-DOF Gantry-Tau design optimisation

The Gantry-Tau design optimisation problem based on the complex search method ([28], [29] and [7]) is expressed as follows.

$$\begin{aligned}
\text{min:} \quad & \mathbf{F} = f_{qual}(\mathbf{par}) + f_{cf}(\mathbf{par}) + f_g(\mathbf{par}) \qquad (45)\\
\text{Subject to:} \quad & Q_4^L(\mathbf{par}) \le Q_4 \le Q_4^U(\mathbf{par})\\
& Q_3^L(\mathbf{par}) \le Q_3 \le Q_3^U(\mathbf{par})\\
& L_3^L(\mathbf{par}) \le L_3 \le L_3^U(\mathbf{par})\\
& L_2^L(\mathbf{par}) \le L_2 \le L_2^U(\mathbf{par})\\
& L_1^L(\mathbf{par}) \le L_1 \le L_1^U(\mathbf{par})\\
& Q_1^L(\mathbf{par}) \le Q_1 \le ISO_{dth}\\
& Q_2^L(\mathbf{par}) \le Q_2 \le ISO_{hth}\\
& 0 \le f_{qual} \le 1\\
& 0 \le f_{cf} \le 1\\
& 0 \le f_g \le 1
\end{aligned}$$

where **par** is a vector of the optimisation variables presented in Sect. 2.

The quality objective function $f_{qual}(\mathbf{par})$ in (45) has $(\frac{m^2}{m^2})$ unit description and includes workspace, collisions between the platform and support frame, installation space, user's specifications. The second objective function $f_{cf}(\mathbf{par})$ has $(\frac{m^2}{m^2})$ units and consists of a sum of both areas where first resonance frequency is lower than required and where the collisions between the links are detected. The constraint handling function $f_g(\mathbf{par})$ has $(\frac{m}{m})$ units and keeps the optimisation

constraints inside of the limits and penalise any infeasible constraints. All objective sub-functions are defined in a range [0; 1] and expressed as follows.

$$f_{qual}(\mathbf{par}) = \frac{IS}{A_R(\mathbf{par}) - A_U(\mathbf{par})} \tag{46}$$

$$f_g(\mathbf{par}) = \frac{\sum_{i=1}^{r} g_i(\mathbf{par})}{r} \tag{47}$$

$$f_{cf}(\mathbf{par}) = \frac{A_f(\mathbf{par}) + A_c(\mathbf{par})}{2UW_aUW_b} \tag{48}$$

$$A_f(\mathbf{par}) = \left\{ \begin{array}{ll} \sum_{i=1}^{NUM} \frac{\delta_i^2}{2UW_aUW_b}, & \text{if } \gamma_{min} > \gamma_i(\mathbf{par}) \\ 0, & \text{if } \gamma_{min} \leq \gamma_i(\mathbf{par}) \end{array} \right\} \tag{49}$$

$$A_c(\mathbf{par}) = \left\{ \begin{array}{ll} \sum_{i=1}^{NUM} \frac{\delta_i^2}{2UW_aUW_b}, & \text{if } L_{Ci} < L_C^* \\ 0, & \text{if } L_{Ci} > L_C^* \end{array} \right\} \tag{50}$$

where $A_R(\mathbf{par})$ is the maximum workspace, $A_U(\mathbf{par})$ is the unreachable area caused by the collisions between the platform and support frame, IS is the installation space and depends on the optimisation parameter Q_4. For the positive Q_4 $IS = Q_2(Q_1 + Q_4)$, for the negative—$IS = Q_2Q_1$. $\gamma_i(\mathbf{par})$ is the first resonance frequency found for the current workspace cell i. $A_c(\mathbf{par})$ is the link collision function and equals 1 if collisions are detected or 0 if there are no collisions for the current workspace cell, δ is the workspace integration parameter, where the minimum workspace cell equals δ^2, NUM is the number of the workspace cells. The dynamics function $A_f(\mathbf{par})$ in (49) is a sum of the workspace cells, when the minimum required first resonance frequency is greater than a current frequency at the given cell. The dynamics objective is also extended by the ratio between the area where the resonance frequency is lower than required and the user's specified workspace. The sum of the workspace cells equals zero, when the required frequency is less than the current for these cells. The installation space depends on the support frame dimensions. The workspace and unreachable area are the functions of five support frame parameters, individual link lengths and platform kinematics. The collisions are detected if the distance between the links L_{Ci} is less or equal to L_C^*. The quality function is minimised while minimising the ratio between the installation space and workspace. The constraints handling method is given below.

$$g_i = 0, \quad \text{if } Par_i^L \leq Par_i^{cur} \leq Par_i^U \tag{51}$$

$$g_i = \left(\frac{Par_i^L - Par_i^{cur}}{Par_i^L} \right)^2, \quad \text{if } Par_i^{cur} < Par_i^L \tag{52}$$

$$g_i = \left(\frac{Par_i^{cur} - Par_i^U}{Par_i^U} \right)^2, \quad \text{if } Par_i^{cur} > Par_i^U \tag{53}$$

where Par_i^{cur} is a current value of the constraint i, Par_i^U is the upper limit and Par_i^L is the lower limit of the constraint i.

The user's specifications included into design optimisation are the minimum first resonance frequency level γ_{min}, minimum distance between two robot's links L_C^*, maximum installation space in the X, Y, Z directions IS_{lth}, IS_{dth} and IS_{hth}, minimum platform radius R_{plmin}, minimum platform length L_{plmin}, joint angles JA, length from the connection point to the centre of the joint L_b, lengths of the tool L_{tool} and pins on the platform L_{pin}, Young's modulus ε, mass of the **TCP** M_{TCP}, mass of the joints M_j, joint stiffness k_j, user's specified workspace in the Y direction UW_a and in the Z direction UW_b, workspace integration step δ. The user's specifications and requirements used in the design optimisation are given in Table 3.

Increasing the first resonance frequency is the main task for the dynamics optimisation. There are some possibilities to increase the resonance frequency. The first possibility is reducing the link lengths while support frame variables Q_1, Q_2 are fixed. The second

Table 3 User's specifications and requirements used in the design optimisation

Parameter	Value	Parameter	Value
L_C^*	0.1 m	γ_{min}	50 Hz
IS_{lth}	2.2 m	IS_{dth}	0.65 m
IS_{hth}	1.2 m	ε	70×10^9 N/m^2
UW_a	0.65 m	UW_b	0.65 m
R_{pmin}	0.07 m	L_{pmin}	0.15 m
k_j	50 N/μm	k_a	232 N/μm
M_{TCP}	5 kg	L_b	0.03 m
M_a	1 kg	L_{pin}	28×10^{-3} m
L_{tool}	1×10^{-3} m	–	–

possibility is increasing the variables Q_1, Q_2 while the link lengths are fixed. The third possibility to increase the stiffness is by shifting the Y position of the actuators T_2 and 3. In this paper the Y position of actuator T_2 is variable while the actuator T_3 position is fixed. The fourth possibility is to change the distances between the points A and B or E, C and D on the platform as well as the platform length. The last way to increase the stiffness in the Y direction is to increase Q_1 while other parameters are fixed. Note, that the support frame parameter Q_1 defines the Y coordinate of the actuator T_1.

7 Results

The final optimised design variables of the 3-DOF Gantry-Tau were found using the complex search algorithm and gradient-based function $fmincon$ available in the Matlab optimisation toolbox. The results are summarised in Table 4 and compared with original and worst designs.

The initial population size is 50 randomised designs. The number of evaluations of the objective function was fixed to 350. However, the number of iterations will be increased when the user's requirements are changed. For example, more iterations are needed when the user specifies more optimisation variables or increases the requirements such as the first resonance frequency level and specified workspace dimensions.

Figure 14 shows the convergence trend of the main objective function **F** as a sum of 3 sub-objectives (f_{qual}, f_{cf} and f_g) in 400 iterations. Figures 15, 16 and 17 show the sub-objective's f_{cf}, f_{qual} and f_g convergency trends in 400 iterations respectively. The quality sub-objective (f_{qual}) depends on kinematic parameters (link lengths and support frame dimensions).

The results would have been difficult to obtain by a manual design, as the support frame dimension is different from $Q_1 = 2Q_2 \approx Q_3$, $Q_4 = 0$ which have been typical manual design choices of the Gantry-Tau in the past. According to Table 4 the objective function was improved by 24%, sub-objectives f_{qual} and f_{cf} by 21%, and 3% respectively. The gradient-based search algorithm is not able to reach a feasible result. The optimised design was obtained in less than 55 hours on a Pentium Centrino 2 (CPU 2.2 MHz) computer. Furthermore, the approach proposed in this paper is relatively simple and can be implemented for other PKMs.

Table 4 Comparison of the design optimisation results

Parameter	Original	Fmincon	Worst	Best
Q_1, m	0.5	0.55	0.54	0.527
Q_2, m	1	1.02	0.99	1.024
Q_3, m	0.42	0.54	0.48	0.36
Q_4, m	0	0.19	0	0.1
L_1, m	1	0.94	1.25	1.11
L_2, m	1	0.95	0.97	0.97
L_3, m	1	0.94	1.21	1.04
F	0.79	0.70	1.58	0.60
f_{qual}, $\frac{m^2}{m^2}$	0.76	0.64	0.59	0.60
f_{cf}, $\frac{m^2}{m^2}$	0.03	0.06	0.98	0
f_g, $\frac{m}{m}$	0	0	0.01	0

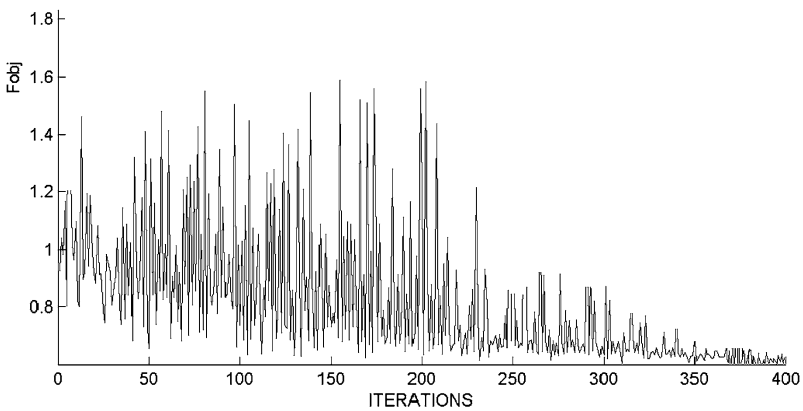

Fig. 14 The convergence trend of the main objective function **F** as a sum of 3 sub-objectives (f_{qual}, f_{cf} and f_g) in 400 iterations

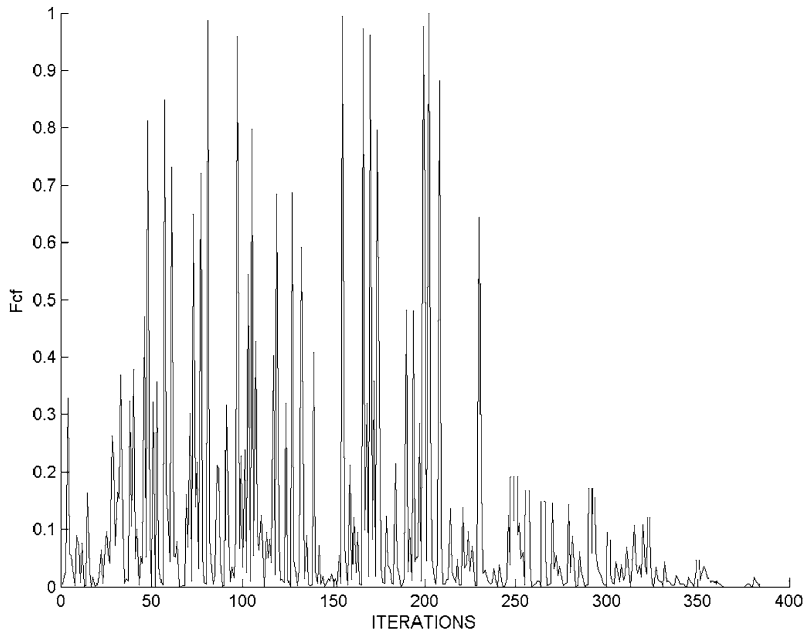

Fig. 15 The convergence trend of the sub-objective function f_{cf} 400 iterations

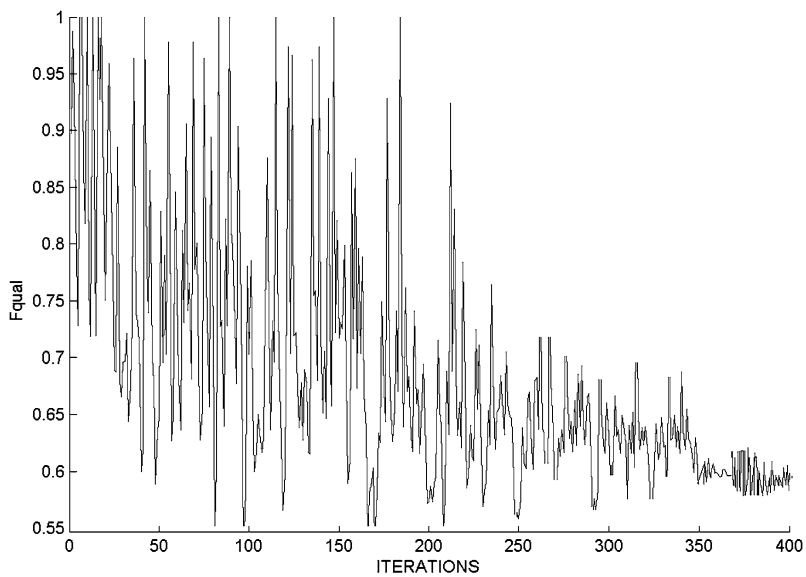

Fig. 16 The convergence trend of the sub-objective function f_{qual} in 400 iterations

8 Conclusions

One of the main contributions of this paper is the combination of the evolutionary multi-objective methodology based on the complex search algorithm with geometric descriptions of the Gantry-Tau to optimise the parallel kinematic structure. The design optimisation scheme includes the kinematic (collisions free workspace) and elastodynamic (first resonance frequency) properties of the PKM as the objectives. The optimisation constraints are the support frame lengths, actuator positions the robot's arm lengths. The design optimisation results show that it is possible to optimise the kinematic design of the Gantry-Tau PKM to

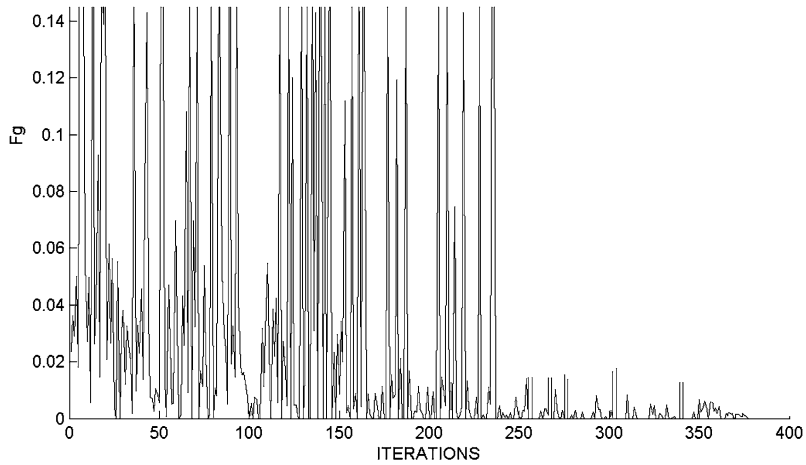

Fig. 17 The convergence trend of the constraints handling function f_g in 400 iterations

achieve a collision-free workspace with the first resonance frequency greater than 50 Hz.

The optimisation results demonstrate the importance of designing PKMs in general and the Gantry-Tau in particular to meet specific end-user requirements. It is therefore important that when the machine is designed, the locations of typical work-objects are known. The machine can then be designed for high performance in these regions. The remaining regions of the workspace with lower performance can typically be used for operations which do not require the machining specifications, such as tool change, docking or work object transfer operations. Dimensional synthesis is a part of the design and to obtain the targeted performance at lowest cost, physical design (material selection, bearing design, actuator design etc.) must also be made. The physical design as a part of the Gantry-Tau design optimisation is one of the future research directions.

Multi-objective evolutionary algorithms require a relatively large number of iterations to produce reasonably good approximations of the optimal set of the designs. This has motivated the hybridisation of evolutionary algorithms (global search engines) with local search engines of different types to reduce the computational time effort.

References

1. Merlet J-P (2000) Parallel robots. Solid mechanics and its applications, vol 74. Kluwer Academic, Dordrecht
2. Gough V (1956–1957) Contribution to discussion to papers on research in automobile stability and control and in tire performance. In: Proc auto div institute of mechanical engineers, pp 392–394
3. Stewart D (1965) A platform with six degrees of freedom. UK Inst Mech Eng Proc 180(15):30–35
4. Brogårdh T (2000) Design of high performance parallel arm robots for industrial applications. In: Proc of the symp comm the legacy, works, and life of sir Robert Stawell Ball, 100th anniv of a treatise on the theory on the screws. Univ of Cambridge, Cambridge
5. Murray M, Hovland G, Brogårdh T (2008) Singularity-free reconfiguration of the 5-DOF Gantry-Tau parallel kinematic machine. In: Proc 2nd intl workshop on fundamental issues and future research directions for parallel mechanisms and manipulators, Montpellier, Sept 21–22
6. Dashy A, Yeoy S, Yangz G, Chery I-H (2002) Workspace anal. and singularity rep. of 3-legged parallel manip. In: Proc 7th intl conf in contr, autom, rob and vision, pp 962–967
7. Tyapin I (2009) Multi-objective design optimisation of a class of parallel kinematic machines. PhD thesis, University of Queensland, Australia
8. Fattah A, Angeles J, Misra A (1995) Dynamics of a 3-dof spatial parallel manipulator with flexible links. In: Proc of the international conference on robotics and automation, pp 627–632
9. Xi F, Sinatra R, Han W (2001) Effect of leg inertia on dynamics of sliding-leg Hexapods. J Dyn Syst Meas Control 123:265. doi:10.1115/1.1369600
10. Lee J, Geng Z (1993) A dynamic model of a flexible Stewart platform. Comput Struct 48:367
11. Hardage D, Weins G (1999) Modal analysis and modeling of a parallel kinematic machine. ASME, Manuf Eng Div 10:857
12. Zhou Z, Xi F, Mechefske C (2006) Modeling of a fully flexible 3PRS manipulator for vibration analysis. J Mech Des 128:403. doi:10.1115/1.2167655

13. Chen J, Hsu W (2006) Dynamic and compliant characteristics of a cartesian-guided Tripod machine. J Manuf Sci Eng 128:494. doi:10.1115/1.1954789
14. Hovland G, Choux M, Murray M, Brogårdh T (2007) Benchmark of the 3-dof Gantry-Tau parallel kinematic machine. In: IEEE intl conf on robotics and automation, pp 535–542. doi:10.1109/ROBOT.2007.363042
15. Dressler I, Robertsson A, Johansson R (2007) Accuracy of kinematic and dynamic models of a Gantry-Tau parallel kinematic robot. In: IEEE int conf on robotics and automation, pp 883–888. doi:10.1109/ROBOT.2007.363097
16. Merlet J-P, Daney D (2008) Smart devices and machines for advanced manufacturing. Springer, London
17. Stamper R, Tsai L, Walsh G (1997) Optimisation of a 3 dof translational platform for well-conditioned workspace. In: Proc IEEE intl conf on robotics and automation, pp 3250–3255. doi:10.1109/ROBOT.1997.606784
18. Gosselin C, Angeles J (1988) The optimum kinematic design of a planar three-degree-of-freedom parallel manipulator. ASME J Mech Transm Autom Des 110(1):35. doi:10.1115/1.3258901
19. Gosselin C, Angeles J (1989) The optimum kinematic design of a spherical three-degree-of-freedom parallel manipulator. J Mech Transm Autom Des 111:202. doi:10.1115/1.3258984
20. Liu X-J, Wang J (2007) A new methodology for optimal kinematic design of parallel mechanism. J Mech Mach Theory 42:1210. doi:10.1016/j.mechmachtheory.2006.08.002
21. Stock M, Miller K (2003) Optimal kinematic design of spatial parallel manipulators: application of linear delta robot. Trans ASME, J Mech Des 292–301. doi:10.1115/1.1563632
22. Chablat D, Wenger P (2003) Architecture optimization of 3-dof translational parallel mechanism for machining applications, the orthoglide. IEEE Trans Robot Autom 19(3):403. doi:10.1109/TRA.2003.810242
23. Liu X-J, Wu C, Wang J (2008) A new index for the performance evaluation of parallel manipulators: a study on planar parallel manipulators. In: Proc of the 7th world congress on intelligent control and automation, pp 353–361. doi:10.1109/WCICA.2008.4592950
24. Lou Y, Liu G, Li Z (2008) Randomized optimal design of parallel manipulators. IEEE Trans. Autom. Sci. Eng. 5(2):223. doi:10.1109/TASE.2007.909446
25. Schaffer J (1984) Some experiments in machine learning using vector evaluated genetic algorithms. PhD thesis, Vanderbilt University, Nashville, TN
26. Wang J, Zhang J, Wei X (2006) Evolutionary multiobjective optimization algorithm with preference for mechanical design. Springer, Berlin, pp 497–506
27. Coello Coello C (2002) Theoretical and numerical constraint-handling techniques used with evolutionary algorithms: a survey of the state of the art. Comput Methods Appl Mech Eng 191(11–12):1245–1287. doi:10.1016/S0045-7825(01)00323-1
28. Hansen M, Andersen T (2001) A design procedure for actuator control systems using optimization methods. In: Proc of the IEEE 7th Scandinavian international conference on fluid power. Linköping, Sweden, pp 213–221
29. Hansen M, Andersen T, Mouritsen O (2004) A scheme for handling discrete and continuous design variables in multi criteria design optimization of servo mechanisms. In: Mechatronics and robotics, Aachen, Germany, pp 234–245
30. Tyapin I, Hovland G (2009) Kinematic and elastostatic design optimisation of the 3-DOF Gantry-Tau parallel kinematic machine. Model Identif Control 30(2):39–56. doi:10.4173/mic.2009.2.1
31. Gosselin C (1990) Determination of the workspace of 6-dof parallel manipulators. ASME J Mech Des 112:331. doi:10.1115/1.2912612
32. Li Y, Kao I (2004) Stiffness control on redundant manipulators: a unique and kinematically consistent solution. In: Intl conf on roborics and automat, pp 3956–3961